Comparing predicted 2D and 3D anisotropic properties from micro CT derived digital rock physics with experimentally measured anisotropy

David K. Potter[1*], *Liam L.* Belisle[1], *Allyson L.* Shewchuk[1], *Brendan C.* Snow[1,2], *Aiden* Zhu[3], and *Shaun* Zhang[3]

[1]Department of Physics, University of Alberta, Edmonton, Alberta, T6G 2E1,Canada
[2]Current address: CNOOC Petroleum North America ULC, Calgary, Alberta, T2G 1A6, Canada
[3]DigiM Solution LLC, Burlington, MA 01803, USA

Abstract. This study compared anisotropic parameters predicted from microcomputed tomography (μCT) derived digital rock physics with experimentally measured anisotropy on the same core plug. Full 3D anisotropy comparisons have not been made previously on a single core plug sample, as far as we are aware, since most experimental methods require several core plug samples cut in different orientations to determine 3D anisotropy. A cloud-based image analysis platform (DigiM I2S) was used to process the μCT scans, with supervised machine learning tools and petrophysics simulations, to produce a digital 3D reconstruction and predict various 3D anisotropic parameters (permeability, electrical conductivity, and acoustic velocity). The results were directly compared with experimentally measured 3D anisotropy of magnetic susceptibility (AMS), anisotropy of magnetic remanence (AMR), and anisotropy of acoustic velocity. A key result was that the orientations of the principal anisotropy axes for the bulk rock components were similar to those of the fine grained ferrimagnetic components. The results were also consistent with the observed petrofabric, giving confidence in the digital rock physics predictions and the rapid 3D experimental measurements, and showed potential for estimating 3D anisotropy of one parameter from measurements or predictions from another parameter on a single core plug (e.g., estimating principal anisotropy axes of permeability, acoustic velocities or electrical conductivity via rapid, non-destructive magnetic anisotropy measurements).

1 Introduction

The major goal of this study is to compare two and three dimensional (2D and 3D) anisotropy parameters from microcomputed tomography (μCT) digital rock physics predictions with experimentally measured anisotropy on the same single core plug. A key factor is the recognition that the digital rock physics methods of Zhang et al. [1, 2] and the magnetic methods of Potter [3] both utilize second order tensors to characterize 3D anisotropic properties of core plugs, thereby allowing direct comparisons between the different methods. Such comparisons have not been made before on a single core plug sample, as far as we know, because most experimental techniques for determining the full 3D anisotropy require several core plug samples cut in different orientations. For example, 3D permeability anisotropy ideally requires 9 plugs cut in different orientations, since the permeability is measured in 1D along the axis of each core plug. In contrast, the magnetic methods of Potter [3] generate the full 3D anisotropy from a single core plug, allowing direct comparison with the 3D digital rock physics parameter predictions on the same sample. The magnetic methods utilized anisotropy of magnetic susceptibility (AMS), which is rapid and represents the combined anisotropy of all the mineral components in the sample, and anisotropy of magnetic remanence (AMR), which reflects the anisotropy of only the fine grained remanence carrying mineral components (generally ferrimagnetic minerals such as magnetite, Fe_3O_4). These different methods allowed us to directly compare the anisotropies of different mineral components and grain size fractions.

A cloud-based image analysis platform (DigiM I2S) was used to conduct image processing of μCT scans of the plug. Supervised machine learning tools and petrophysics simulations were used to predict anisotropies of permeability, electrical conductivity, and s-wave velocity from the μCT scans. The results were compared with experimentally measured AMS, AMR, and s-wave velocity anisotropy.

2 Sample description

The sample used in this study was part of the VOLC-B ("volcanic" B) group of outcrop igneous rock samples [4] from the Flin Flon Belt of the Trans-Hudson Orogeny in eastern Saskatchewan. These rocks have been studied due to the economic potential of their mineral deposits. **Figure 1** shows the sample with the arbitrary reference X, Y and Z axes indicated. Analysis [4] suggested that this group of rock samples was composed of 22.5% quartz, 61.2% plagioclase, 8.3% biotite, and 1.9% opaque minerals (the remaining 6.1%

* Corresponding author: dkpotter@ualberta.ca

being porosity and/or some other small unidentified minerals). The cylindrical plug sample used for the present study, VOLC-B-X2, had a mass of 27.46 g and a density of 2.635g/cm^3. The sample was initially thought to be quasi-isotropic [4] from some preliminary acoustic analysis. However, the current study will demonstrate that the sample is clearly anisotropic. We specifically chose this sample as it had a visible petrofabric that could be compared with the quantitative anisotropy methods. Whilst this is not a typical reservoir rock, it represents a good sample to test all the different methods, since some techniques may not produce sufficient signal in certain sedimentary rocks.

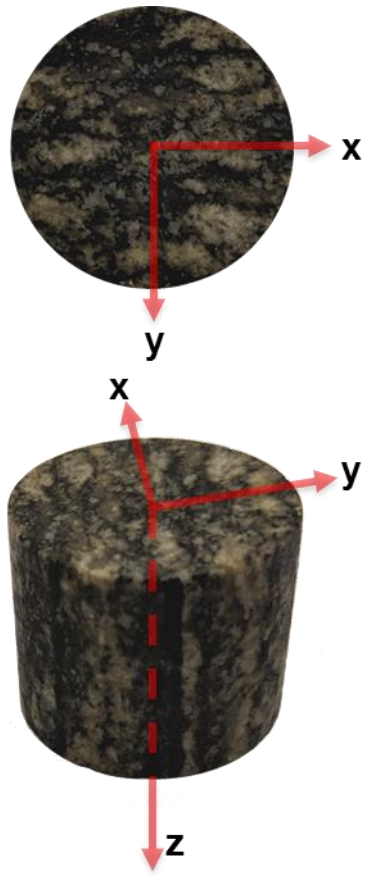

Fig. 1. Images of core plug sample VOLC-B-X2 showing the orientations of the arbitrary orthogonal reference axes X, Y and Z. **Top:** top view of the sample showing the XY plane (the directions of the arrows indicate the positive X and Y directions, and positive Z is into the page). The diameter of the circular XY plane is 25 mm. **Bottom:** side view of the sample showing the positive directions of all 3 orthogonal axes. The orientations of the axes in terms of declination (Dec.) and inclination (Inc.) are as follows: X has Dec. 0º and Inc. 0º, Y has Dec. 90º and Inc. 0º, and Z has Dec. 0º and Inc. 90º.

3 Methods

3.1 Micro CT imaging and digital rock physics predictions of anisotropic properties

Microcomputed tomography (µCT) imaging with a voxel resolution of 10.7 µm was used to create a series of digital images in order to build up a comprehensive 3D representation of the core plug sample, and to distinguish its main components. After some quality control, where a few low quality images were removed, the final dataset consisted of 1,500 good quality images taken in the XY plane along the Z axis. These were used to produce a 3D reconstruction at 10.7 µm voxel resolution of the majority of the sample. The numerical domain for the reconstruction and the subsequent modelling was a cubic volume 18 mm x 18 mm x 18 mm. The image contrast and saturation were enhanced in order to help accentuate fine details. The density of a mineral phase in the µCT images was represented by the contrast; a higher contrast indicated a higher density (a lighter grayscale shade in the initial images, which was later replaced by different colours). Image segmentation was conducted to create four different main components within each image, using a machine learning supervised random forest classifying algorithm [5]. The image segmentation module was first trained on a representative sample image taken from the middle of the dataset to distinguish the four main components found in the anisotropic rock: quartz, plagioclase, biotite and porosity. Then, using this training set, the image segmentation module classified every voxel in the dataset under one of the four components. Given its high density, voxels with the highest image contrast were considered biotite. Likewise, given its low density, voxels with the lowest image contrast (darkest grayscale) represented the porosity. The fluid in the pores was assumed to be air, though there is the possibility that some fluid inclusions may be present. Voxels representing the lighter intermediate shade were considered plagioclase, and voxels representing the darker intermediate shade were considered quartz, since labradorite plagioclase has a higher density than quartz. Since there was no immediate way to differentiate the small amount of opaque minerals from the other mineral components in the µCT images (the resolution was not high enough to identify some of these micron sized grains), we assumed only plagioclase, quartz, biotite and porosity in the µCT images. These formed the four components of the anisotropic rock classifier. Our magnetic measurements suggested that at least one the opaque minerals likely comprised ferrimagnetic magnetite or titanomagnetite. For this study, it was assumed that the identified minerals exhibited no compositional variations within the anisotropic rock.

A cloud-based image analysis platform (DigiM I2S) was then used to predict the principal anisotropy axes of the 3D digitally reconstructed core plug sample for various physical parameters (permeability, electrical conductivity and s-wave velocity) by running different software modules on the segmented datasets. For the permeability module, the segmented dataset was loaded in and porosity was chosen as the “active” material. The module seeks to represent the pores as a finite volume mesh. Stoke’s and Darcy’s equations are then solved for the constructed complex pore network. The simulations virtually push fresh water through this network with a pressure difference of 30,000 Pa [1], producing a 9 component (3 diagonal components and 6 off-diagonal

components) permeability second order tensor [1, 2], from which full 3D anisotropy is calculated giving the magnitudes and orientations of the 3 principal anisotropy axes (maximum, intermediate and minimum).

The electrical conductivity module solves Laplace's equations on a multi-component sample with each component assigned an electrical conductivity value as follows [6]: Biotite: 2.5 mSm^{-1}, Plagioclase: 0.01 mSm^{-1}, Quartz: 0.0 mSm^{-1}, Porosity: 0.0 mSm^{-1} (note that whilst quartz has an extremely small, non-zero, electrical conductivity, the software had a tolerance threshold which meant quartz had to be assigned a zero value). The electrical conductivity module presently only predicts values along individual axes, so we predicted values along the X, Y and Z reference axes (i.e., in three orthogonal orientations) to obtain an estimate of the 3D anisotropy. This process can, if necessary, be repeated in 3 different orthogonal axes to improve the estimate.

The electrical conductivity module was also adapted to predict s-wave velocity values along the X, Y and Z reference axes. S-wave velocities were assigned as follows [7]: Biotite: 1,360 ms^{-1}, Plagioclase: 3,728 ms^{-1}, Quartz: 4,200 ms^{-1}, Porosity: 0 ms^{-1}.

3.2. Magnetic anisotropy

3.2.1 Anisotropy of Magnetic Remanence (AMR)

AMR methods measure the anisotropy of just the remanence carrying minerals (generally fine particles of ferrimagnetic minerals such as magnetite, or canted antiferromagnetic particles such as hematite), and thus quantify the anisotropy of part of the small fraction of "opaque" minerals. This can be important since such minerals can influence the permeability anisotropy [3, 8]. Two methods were used: (i) anisotropy of isothermal remanent magnetization (AIRM), and (ii) anisotropy of gyroremanent magnetization (AGRM). We firstly chose AIRM primarily because the technique produces 9 components representing a second order tensor [3, 9, 10] that was similar to that used to predict permeability anisotropy from μCT images [1, 2] described earlier. This meant that for the first time the 3D permeability anisotropy predicted from μCT images could be directly compared with experimental measurements of AIRM on an identical single core plug. Also, AIRM measurements can be made at room temperature to avoid any chemical changes, and they give a large signal compared to other AMR techniques. The sample was first tumble AF demagnetized and then placed in a Molspin pulse magnetizer, which applied a short (100ms) direct field (DF) in a specific orientation. This imparted an IRM, which was measured in a spinner magnetometer, giving 3 components of magnetization. The DF was applied successively along the X, Y, and Z axes and the IRM measured each time, giving a total of 9 components of magnetization as follows:

DF Axis	Measured Remanence	
X	M_{1x} M_{1y} M_{1z}	
Y	M_{2x} M_{2y} M_{2z}	(1)
Z	M_{3x} M_{3y} M_{3z}	

Between each measurement the sample was tumble AF demagnetized. A typical AIRM determination from the 3 magnetization and 3 demagnetization steps takes around 20-30 minutes. The 9 components of magnetization represented a second order tensor from which the magnitude and orientation of the 3 principal anisotropy axes could be calculated [3, 9, 10]. The AIRM measurements were made at two different DF values, 60mT and 20mT, in order to quantify the anisotropy of different particle size fractions. The higher field preferentially affects the small (generally submicron) stable single domain (SSD) ferrimagnetic particles, whilst the lower field preferentially affects the slightly larger (generally up to a few tens of microns) multidomain (MD) ferrimagnetic particles.

AGRM is another AMR method and is produced when an anisotropic distribution of SSD ferro- or ferrimagnetic particles are subjected to an AF with the sample static [10, 11, 12]. It is not theoretically produced in MD particles and so can exclusively quantify the anisotropy of the SSD particles. GRM is produced perpendicular to both the AF axis and the maximum alignment orientation of the particles. This method applies an AF to the static sample at various orientations in 3 orthogonal planes. This was achieved using an AF demagnetizer coil housed within a mumetal shield. The latter shielded the sample from the Earth's field. The sample was subjected to an AF of 60 mT at increments of 15° within a 180° range (from θ = -90° to 90°) in a particular plane (**Figure 2**). After the AF application, the sample was removed from the AF coil and the GRM components (x, y and z) were measured in a spinner magnetometer. Prior to each AF application the sample was tumble AF demagnetized at 80 mT and the remaining remanence measured, and subtracted from the subsequent GRM measurement. The demagnetizing field was higher than the AF used to impart the GRM in order to remove as much remanence as possible prior to each GRM production step. Thirteen pairs of magnetized and demagnetized values were obtained in the 3 orthogonal planes (XY, YZ, and ZX) giving a total of 39 measurements of GRM. The first axis letter of each plane has an orientation of θ = 0º and the second axis letter of the plane has an orientation of θ = 90º (e.g., for the XY plane the X axis is oriented at θ = 0º and the Y axis is oriented at θ = 90º). The GRM method is extremely sensitive, but quite time consuming, taking a few hours to perform. It is effectively the remanence equivalent of the anisotropy of magnetic susceptibility (AMS) delineator (see the AMS section below), since it measures the differences in anisotropy of the SSD ferro- or ferrimagnetic particles in a particular plane. The magnitude of the GRM is proportional to the anisotropy of the SSD particles in the perpendicular plane [12]. The GRM method does not give the magnitudes of the principal anisotropy axes, since there is no "bulk" value (unlike AMS) to add to the differences. Therefore this method does not produce an anisotropy ellipsoid (unlike the AMS and AIRM methods), but instead the results from each plane can be fit using a standard least-squares algorithm to determine the order (i.e., max, int, and min.) and orientations of the principal anisotropy axes [10].

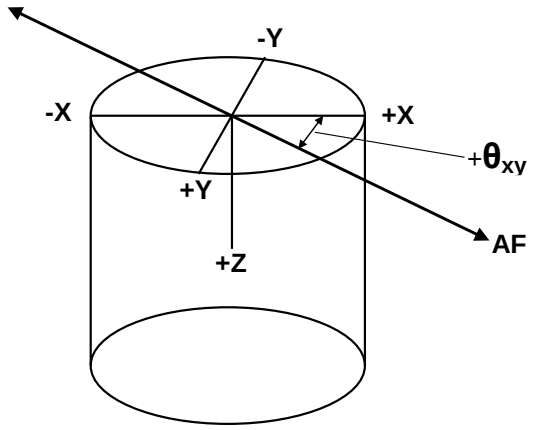

Fig. 2. An example showing the orientation of the AF axis with respect to the sample reference axes during determination of AGRM. The example shows the AF axis at an angle $+\theta_{xy}$ in the XY plane of the sample. This produces a GRM in the Z axis if the sample contains anisotropically distributed SSD ferrimagnetic particles in the XY plane.

3.2.2 Anisotropy of Magnetic Susceptibility (AMS)

This method was quickest to conduct and produced a full 3D anisotropy ellipsoid, and so could be compared exactly with the predicted 3D permeability anisotropy from the μCT imaging and the 3D anisotropy from the AMR methods (AIRM and AGRM). The sample was first demagnetized by tumbling in an alternating field (AF). It was then placed in a Molspin anisotropy delineator, where the sample was rotated successively in the XY, YZ, and ZX planes in a weak magnetic field (500 μT), and the difference in magnetic susceptibility in each plane was measured. The rotations allow the weak field to interrogate all possible orientations in each of the 3 orthogonal planes, and the whole process only takes about 1 minute. A bulk magnetic susceptibility measurement was then added to each of these magnetic susceptibility differences in order to produce the magnitudes and orientations of the 3 principal AMS axes. The bulk measurement was taken separately in a Molspin susceptibility bridge by first measuring the background and then the sample magnetic susceptibility in the Z axis. These bulk measurements take less than about 5 s. The AMS represents the sum total of the anisotropies of all the components in the sample. It can be dominated by small amounts of fine-grained remanence carrying particles (such as ferrimagnetic magnetite, Fe_3O_4), which contribute to the "opaque" minerals as mentioned earlier. If these particles are predominantly stable single-domain (SSD) then the maximum magnetic susceptibility will be perpendicular to the long axes of the particles [9, 13], but if they are slightly larger and multidomain (MD) then the maximum magnetic susceptibility will be along the long axes of the particles [9, 13]. Therefore AMS alone may not unambiguously indicate the orientation of these particles (without knowing the domain state). However, a combination of AMS and AMR methods allows one to uniquely determine the predominant domain state and the correct orientation of the particles [9, 13].

3.3. Anisotropy of shear-wave velocity (ASWV)

Parallel planar transducers, placed on the two flat circular faces of the cylindrical core plug sample, can only measure the p-wave velocity along the cylinder axis (i.e., in 1D along the Z axis) and thus cannot measure 3D anisotropy. However, 2D measurements of s-wave anisotropy were possible in the XY plane. Two parallel planar piezoelectric transducers were attached to aluminium endcaps (calibrated for the extra travel time of the signal through them) and copper electrodes by conductive silver epoxy. The endcaps were placed on the flat end faces (in the XY plane) of the sample, and good coupling was achieved via a thin film of molasses. The frequency of the signal was 1 MHz. While the overall wave train propagated along the Z axis, the s-waves had a transverse motion in the perpendicular XY plane. By rotating the sample in the XY plane with respect to the transducers, using the method described in [14], it was possible to detect s-wave anisotropy in the XY plane. An s-wave was first propagated with the sample at a particular orientation in the XY plane, and the arrival time was recorded manually. Then the sample was rotated through 22.5° in the XY plane and an s-wave was again recorded, and the process repeated every 22.5° as the XY plane was rotated about 360°. The s-wave velocities were determined at each orientation to create a 2D plot of the s-wave velocity anisotropy in the XY plane. The results could be compared to the AGRM in the XY plane, the s-wave predictions from the μCT imaging, and the other anisotropy data.

4 Results and discussion

4.1. Digital 3D reconstruction from the μCT images

Figure 3 shows representative digital reconstructions in the 3 orthogonal XY, YZ and ZX planes derived from the μCT images. One can clearly see that the petrofabric is oriented more towards the X axis in the XY plane, and more towards the Z axis in the YZ plane, whilst the preferred orientation in the ZX plane is less obvious. This indicates that the bulk minerals are aligned more along the X and Z axes than the Y axis, and that the anisotropy in the ZX plane is lower than in the XY and YZ planes. These observations will be shown to correlate with the quantitative anisotropy results for the different parameters detailed later. Another interesting observation is that almost all the modeled porosity appears to be in the quartz, though there may be additional micro porosity that was below the resolution of the μCT images.

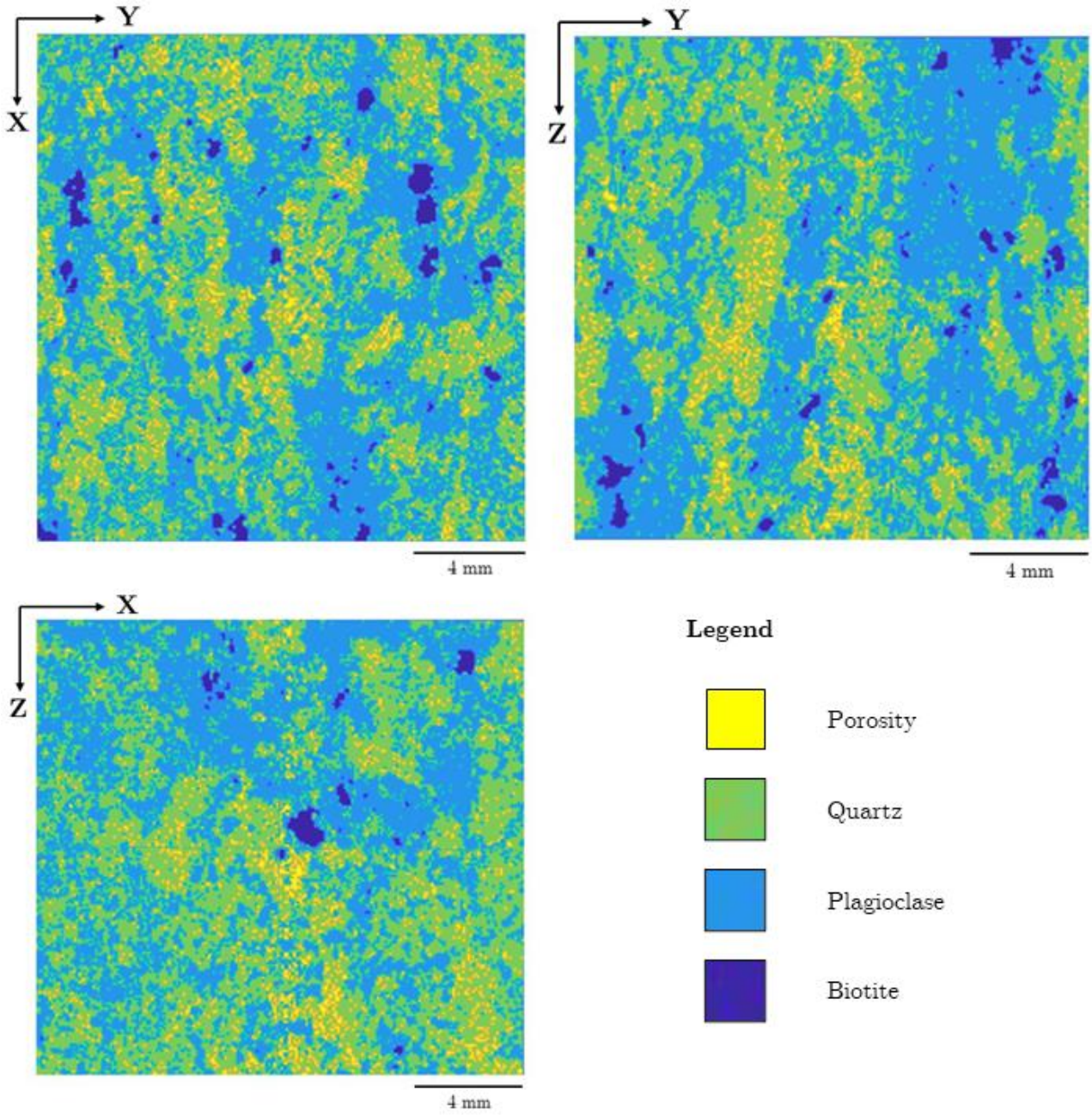

Fig. 3. Digital reconstructions in the 3 orthogonal XY, YZ and ZX planes derived from the μCT images. The 2D orientations of the sample axes are shown in each image. The density contrasts from the μCT images were used to classify 4 main components as shown. The digital reconstructions used the following filters: Gaussian blur, difference of Gaussians, Hessian and Sobel. In the XY plane the minerals are generally more aligned along the X axis, whilst in the YZ plane they are generally more aligned along the Z axis. In the ZX plane the alignments are less pronounced. These observations are consistent with the petrofabric alignments described earlier from the whole plug images shown in **Figure 1**. An interesting observation is that virtually all the predicted porosity (that which can be resolved in these reconstructions) appears to reside in the quartz. There may be additional porosity at a smaller scale that was below the resolution of the initial μCT images.

4.2. Comparisons of 3D anisotropies from μCT imaging predictions and experimental measurements

Table 1 compares the full 3D anisotropy results for the permeability anisotropy predicted from the μCT imaging with the experimentally measured AIRM at 20 mT and 60 mT. Both these methods use an identical 9 component second order tensor scheme to calculate the anisotropy, and so can be directly compared on a single core plug for the first time (as far as we are aware). The results from each method gave quite similar orientations for the 3 principal anisotropy axes, which were relatively close to the X, Y and Z reference axes of the sample, and showed that in terms of magnitudes Z>X>Y. Some differences in the orientations of the principal anisotropy axes between the two methods may be due to the permeability being related to the orientation of the quartz grains, where most of the predicted porosity resides, whereas the AIRM represents the alignments of the small remanence carrying particles. Also, since the permeability values are quite low, any small variation in the off-diagonal terms will affect the overall orientations. The normalized magnitudes of the two AIRM determinations were quite similar, with the anisotropy at 20 mT being slightly larger than that at 60 mT. This may be partly due to the non-linear acquisition of IRM with applied field strength (which accentuates the anisotropy at lower fields), and/or the shape of the larger MD particles may be more elongate, and/or the MD particles may be slightly more aligned than the SSD particles. The normalized magnitudes of the permeability anisotropy show that the permeability is slightly more anisotropic than the AIRM, though the maximum normalized value is quite similar to that of the AIRM.

Table 1 shows that the orientations of the AMS principal axes are also very similar to the orientations of the AIRM and permeability principal axes. The normalized magnitudes of the AMS axes are quite similar to those of the AIRM axes, though they indicate that the AMS is slightly smaller than the AIRM. This can be explained by SSD and MD particles being aligned in the same orientation (which the 60 mT and 20 mT AIRM results respectively demonstrate), since the magnetic susceptibility of SSD particles is a minimum in the alignment axis, whereas for MD particles it is a maximum in the alignment direction [9, 13]. Therefore the AMS of the two sets of particles partially cancels out resulting in lower AMS than AIRM.

The results for this sample suggest that the data from any one of the parameters (AIRM, AMS or permeability anisotropy) could potentially be used to predict the orientations of the principal anisotropy axes of any of the other parameters. In particular, AMS and AIRM could potentially provide rapid, non-destructive indications of the orientations of the principal permeability axes on a single core plug, something that would otherwise be very time consuming to measure experimentally since it would require permeability to be determined by several core plugs cut in different directions (ideally 9 plugs, each measuring the permeability in 1D).

Table 1 also indicates how the SSD ferrimagnetic particles are aligned from the anisotropy of GRM (AGRM) results (in terms of maximum, intermediate and minimum) in relation to the reference X, Y and Z axes of the sample. Since the sample acquires a GRM then the SSD particles are very likely to be magnetite or titanomagnetite (since hematite does not acquire GRM). Whilst this method does not give magnitudes for the principal axes (as detailed in the Methods section), it does indicate the maximum and minimum axes and their orientations in each of the 3 orthogonal planes measured. **Figure 4** shows the GRM values (open data symbols with uncertainty bars) acquired along the Z, X and Y axes following application of an AF of 60 mT in the XY, YZ and ZX planes respectively (GRM is acquired along an axis perpendicular to the plane in which the AF is applied). Least squares best fit curves were drawn for each plane of measurements and demonstrated that the GRM largely followed a sin (2θ) shape in each case in accordance with GRM theory [11], where θ was the orientation of the applied AF as shown in **Figure 2**. The solid symbol on the best fit curve in each plane in **Figure 4** indicates the maximum GRM on that curve. According to GRM theory [11] the predominant alignment orientation of the ferrimagnetic SSD particles in each plane is 45º from the maximum GRM on the positive slope part of the best fit curves. The GRM results indicate that in the XY plane the predominant alignment of the SSD particles is close to the X direction (actually at θ = 11.7º where X is at θ = 0.0º), and in the YZ plane the predominant alignment of these particles is close to the Z direction (actually at θ = 82.1º where Z is at θ = 90.0º). Therefore the SSD particles are aligned more in the X and the Z axes than in the Y axis. The maximum GRM is also greater in the YZ plane than in the XY plane, which shows that the SSD particles are preferentially more aligned along the Z axis than the X axis. The maximum GRM in the ZX plane occurs at a negative value of θ, which is also consistent with the SSD particles being more aligned along Z than X. The GRM values in the ZX plane are small indicating that there is less of a difference between the Z and X axes than between either of these axes and the Y axis. Thus the AGRM indicates Z>X>Y, which is consistent with the predicted permeability anisotropy, and the measured AIRM and AMS results.

Also shown in **Table 1** are the predicted anisotropy results for electrical conductivity and s-wave velocity derived from the μCT images. Whilst these techniques presently do not give the full 3D anisotropy ellipsoid (as detailed in the Methods section) they nonetheless give the predicted values in the 3 orthogonal axes X, Y and Z, which is a reasonable approximation to the 3D anisotropy. Each of these methods also show that in terms of magnitudes Z>X>Y, which is consistent with all the other anisotropy results even though the normalized magnitudes differ somewhat.

The combined results in **Table 1** show that the anisotropy of the major mineral components (from the μCT predicted anisotropies of permeability, electrical conductivity, s-wave velocity, and the observed petrofabric in **Figures 1** and **3**) has a very similar orientation to the fine-grained ferrimagnetic particles (from the AIRM, AGRM and AMS results).

Table 1. The principal 3D anisotropy axes of sample VOLB X2 from different digital rock physics µCT imaging predictions and experimental measurements. For the permeability anisotropy, AIRM and AMS the full 3D anisotropies were determined. The AGRM measurements in each plane (see text and **Figure 4**) allowed determination of the max., int. and min. axes. The electrical conductivity and s-wave velocity predictions were made along each of the 3 orthogonal X, Y and Z axes without the off-diagonal components. Units for the magnitudes are as follows: permeability (mD); AIRM (10^{-6}A m^3kg^{-1}); AMS (10^{-8} m^3kg^{-1}); electrical conductivity (mSm^{-1}) s-wave velocity (ms^{-1}). Magnitudes are not applicable (N/A) for the AGRM as explained in the text. The orientations of the principal anisotropy axes are generally relatively close to the sample axes, where X has Dec. (declination) 0º and Inc. (inclination) 0º, Y has Dec. 90º and Inc. 0º, and Z has Dec. 0º and Inc. 90º. Note that Dec. 0º is the same as Dec. 360º.

ANISOTROPY METHOD	**9-Component Tensor** $\begin{bmatrix} xx & xy & xz \\ yx & yy & yz \\ zx & zy & zz \end{bmatrix}$	**Principal Anisotropy Axes**			
		Magnitudes		**Normalised magnitudes**	**Dec. (º)**	**Inc. (º)**
Permeability anisotropy from µCT	$\begin{bmatrix} 1.367 & -0.011 & 0.015 \\ -0.009 & 0.289 & 0.052 \\ 0.016 & 0.021 & 1.387 \end{bmatrix}$	Max.	1.40	0.46	3.1	62.4
		Int.	1.36	0.45	358.4	-27.5
		Min.	0.29	0.09	89.4	-1.9
AIRM at 20mT	$\begin{bmatrix} 35645 & 3765 & -132 \\ 209 & 18984 & 1752 \\ 2675 & 7931 & 42218 \end{bmatrix}$	Max.	43428	0.45	43.5	73.5
		Int.	35470	0.37	3.3	-12.8
		Min.	17950	0.18	95.6	-10.3
AIRM at 60mT	$\begin{bmatrix} 71810 & -3082 & -438 \\ 5719 & 50343 & 4274 \\ 3403 & 5206 & 83277 \end{bmatrix}$	Max.	84167	0.41	47.0	78.8
		Int.	71643	0.35	1.8	-8.0
		Min.	49620	0.24	92.9	-7.9
AMS	N/A	Max.	2721	0.39	52.3	75.0
		Int.	2478	0.36	8.3	-10.9
		Min.	1698	0.25	100.2	-10.2
AGRM	N/A	Max. (Z)	N/A	N/A	N/A	N/A
		Int. (X)	N/A	N/A	N/A	N/A
		Min. (Y)	N/A	N/A	N/A	N/A
Electrical conductivity anisotropy from µCT	N/A	Max. (Z)	3.670	0.54	0.0	90.0
		Int. (X)	2.194	0.32	0.0	0.0
		Min. (Y)	0.966	0.14	90.0	0.0
S-wave velocity anisotropy from µCT	N/A	Max. (Z)	3610	0.336	0.0	90.0
		Int. (X)	3576	0.333	0.0	0.0
		Min. (Y)	3546	0.330	90.0	0.0

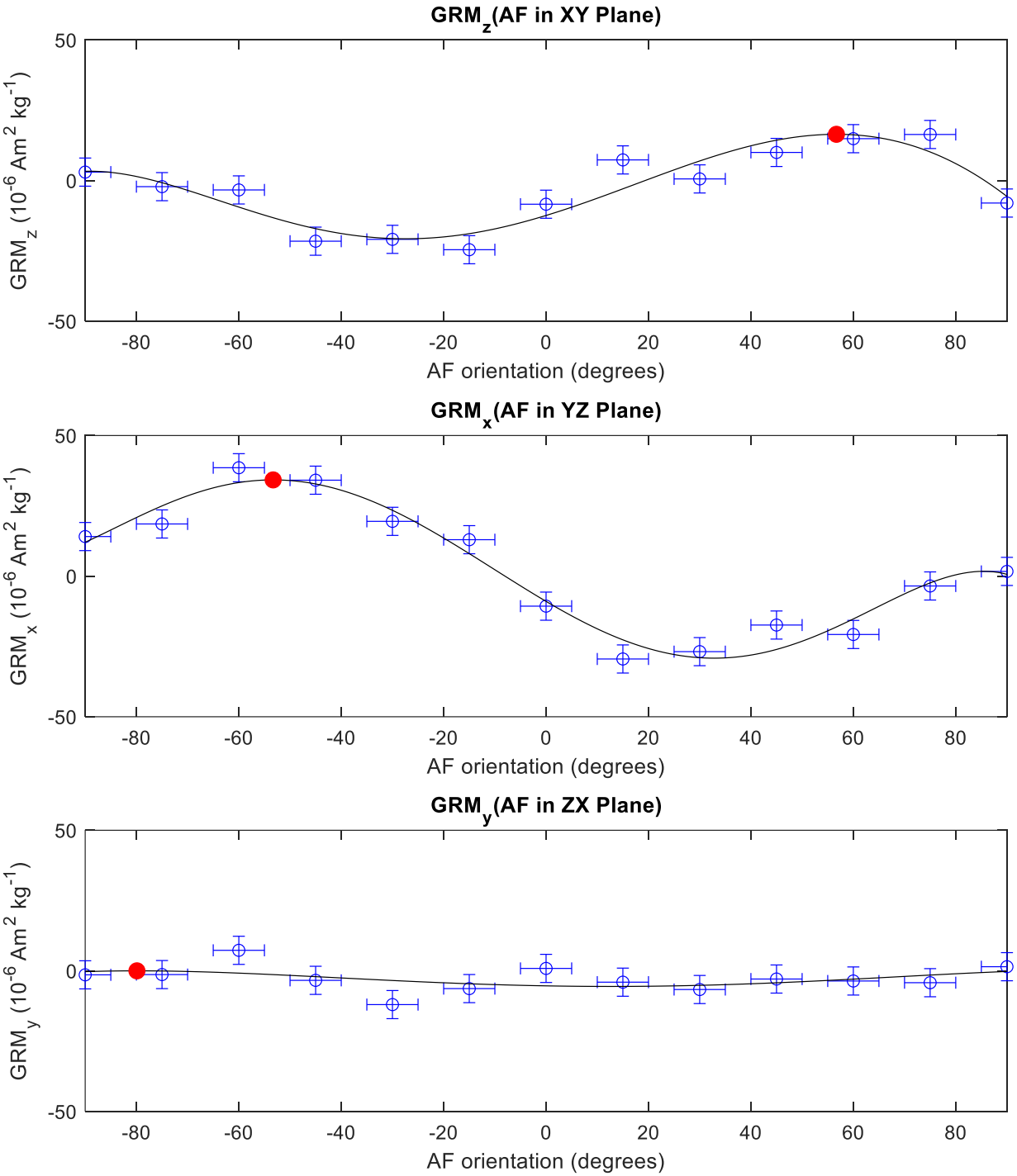

Fig. 4. Components of GRM as a function of AF orientation (θ) in the 3 orthogonal planes. The first axis letter of the plane has an orientation of θ = 0º and the second axis letter of the plane has an orientation of θ = 90º (e.g., for the XY plane the X axis is oriented at θ = 0º and the Y axis is oriented at θ = 90º). The smooth curves are the best fit sin (2θ) curves to the experimental data points. The solid circular point on each plane's best fit curve represents the maximum GRM on that curve. **Top:** The z-components of GRM for orientations of the AF axis in the XY plane. From GRM theory [11] a positive GRM for positive angles of θ means that X>Y in this plane. The GRM results indicate that the predominant alignment of the SSD ferrimagnetic particles in this plane is at θ = 11.7º (45º away from the maximum GRM where the GRM is zero according to GRM theory [11]). **Middle:** The x-components of GRM for orientations of the AF axis in the YZ plane. A positive GRM for negative angles of θ means that Z>Y in this plane. The predominant alignment of the ferrimagnetic particles in this plane is at θ = 82.1º. **Bottom:** The y-components of GRM for orientations of the AF axis in the ZX plane. The slightly more positive GRM (on average) for negative angles of θ means that Z>X in this plane. However, the difference between the Z and X axes is quite small. Compared to the uncertainties shown it is difficult to estimate the predominant alignment of the ferrimagnetic particles in this plane.

4.3. Anisotropies in the XY plane: comparison of µCT predictions and experimental measurements from 2D and 3D results

Since we were able to measure the s-wave velocity anisotropy and the AGRM in the XY plane, it is useful to directly compare these results with the µCT predicted anisotropies of s-wave velocity, permeability and electrical conductivity in the XY plane, as well as the measured AIRM and AMS. **Figure 5** shows the 2D s-wave velocity results (diamond symbols) in the XY plane from [14] and the solid line represents a subsequent best fit curve that we added using a least squares fitting method. This curve forms a "figure of 8" pattern, demonstrating anisotropy in the XY plane. If the sample had been isotropic in the XY plane then the results would have formed a circle. On the best fit line the declination of the maximum s-wave velocity axis was at 12.6° (i.e., close to the X axis at 0° or 360º) with a magnitude of 3,033 ms^{-1} (upper circular point). The minimum s-wave velocity axis was at 103.1° (i.e., close to the Y axis at 90° or 270º) with a magnitude of 2,976 ms^{-1} (lower circular point). The s-wave results did not form a perfectly symmetrical "figure of 8", possibly due to slight differences in the coupling of the transducers to the sample during each experimental measurement.

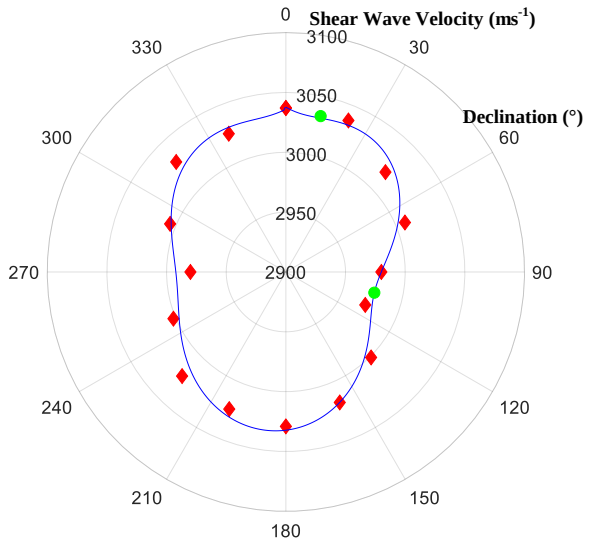

Fig. 5. Shear wave velocities for sample VOLC-B-X2 modified from [10]. The radius axis is the shear wave velocity in ms^{-1} and the circumferential axis is the declination in degrees. The diamonds represent the data points measured by Snow [14]. Measurements were taken by rotating the sample at 22.5° intervals in the XY plane between planar transducers. The solid "figure of 8" line is a least squares best fit of the diamonds, and the two circular points on the best fit line are the maximum and minimum points of the best fit line.

Table 2 shows that the predicted s-wave velocity anisotropy from the µCT imaging was consistent with the X axis velocity higher at 3,576 ms^{-1} than the Y axis velocity of 3,546 ms^{-1}. The measured velocities are lower than the predicted values, possibly due to small micro fractures in the sample below the resolution of our µCT images. Any extra porosity is not included in the estimations from our images, which would make our predicted s-wave velocities higher than the measured values. Our digital reconstructions from the µCT images suggested only 3.4% porosity, but the data of [4] suggested up to 6.1% porosity (though this value may be lower if small amounts of unidentified minerals are present) in the VOLC-B rocks that included our sample.

Table 2. The maximum and minimum principal anisotropy axes in the XY plane from several different methods (digital rock physics predictions and experimental measurements). The 2D determinations all have zero inclinations (0.0 º Inc.) since only the 2D XY plane was considered. The 3D determinations show the two principal axes nearest to the XY plane for comparison from full 3D determinations. Axes listed "Max. (X)" and "Min (Y)" for some of the predictions mean determinations were only made along those axes. Units for the magnitudes are as follows: s-wave velocity (ms^{-1}); permeability (mD); AMS (10^{-8} m^3kg^{-1}); AIRM (10^{-6}A m^3kg^{-1}); electrical conductivity (mSm^{-1}). Magnitudes are not applicable (N/A) for the AGRM as explained in the Methods section in the text.

Method in XY plane	Axis and magnitude	Dec. (°)	Inc. (°)
S-wave velocity (2D measurements)	Max. 3,033	12.6°	0.0°
	Min. 2,976	103.1°	0.0°
S-wave velocity via µCT imaging (3D predictions)	Max. (X) 3,576	0.0°	0.0°
	Min. (Y) 3,546	90.0°	0.0°
AGRM (2D measurements)	Max. (mag. N/A)	11.7°	0.0°
	Min. (mag. N/A)	101.7°	0.0°
Permeability via µCT imaging (3D predictions)	Max. 1.36	358.4°	-27.5°
	Min. 0.29	89.4°	-1.9°
AMS (3D measurements)	Max. 2,478	8.3°	-10.9°
	Min. 1,698	100.2°	-10.2°
AIRM at 60mT (3D measurements)	Max. 71,643	1.8°	-8.0°
	Min. 49,620	92.9°	-7.9°
AIRM at 20mT (3D measurements)	Max. 35,470	3.3°	-12.8°
	Min. 17,950	95.6°	-10.3°
Elect. Conductivity via µCT imaging (3D predictions)	Max. (X) 2.194	0.0°	0.0°
	Min. (Y) 0.966	90.0°	0.0°

Table 2 shows that the orientations of the maximum and minimum principal anisotropy axes from the experimentally measured s-wave anisotropy results (declinations 12.6° and 103.1°) are almost identical to those of the AGRM results (declinations 11.7° and 101.7°). The s-wave results show that the overall rock anisotropy of the main rock forming minerals (plagioclase and quartz) in the XY plane therefore has quite a similar orientation to that of the small fraction of SSD ferrimagnetic particles from the AGRM results.

A comparison of all the anisotropy results for the XY plane in **Table 2** shows that the declinations and inclinations of the maximum and minimum principal axes are quite similar for all the methods. For the results based on 2D data the inclinations are nominally 0.0° since no information in the third dimension is included. For the results based on 3D methods we give the maximum and minimum principal axes (which were very close to the XY plane) based on the full 3D data, and so these determinations include small inclinations in most cases. The results demonstrate that the orientations of the fine SSD and MD ferrimagnetic particles (from the AGRM, AIRM and AMS results) are quite similar to those of the main rock forming minerals plagioclase and quartz (from the measured and predicted s-wave velocity anisotropy, the predicted electrical conductivity as well as the visible petrofabric in **Figures 1** and **3**). Whilst there is a close correspondence between the orientation results for the different methods for this sample, it may not always be the case for other core samples and rock types. The advantage of performing all the different methods described here is that it allows one to determine the anisotropy of the different components (minerals and pore network) and, in the case of the ferrimagnetic fraction, different particle size fractions (SSD versus MD).

5 Discussion

A main aim of this paper was to highlight that the digital rock physics predictions and certain experimental anisotropy techniques (AMS and AIRM) both utilize an identical second order tensor approach, thus allowing direct comparisons of the full 3D anisotropy from the different methods on exactly the same cylindrical core plug. The igneous sample we chose also allowed us to compare many different anisotropy techniques on the same plug, and relate the results to the observed petrofabric. We recognize that the methodology and assumptions employed in the digital physics permeability module are more applicable to sedimentary rocks. Nevertheless we demonstrated that the digital physics predicted principal permeability axes corresponded quite well (in terms of orientations and normalised magnitudes) to the AIRM, AMS and other anisotropy results. This suggests that the digital rock physics predictions do have some physical meaning in this case. Whether the permeability anisotropy results are realistic for our igneous sample is open for discussion. It is not currently possible (with present technology) to measure the full 3D permeability anisotropy on a single cylindrical core plug in order to verify our predictions. Experimental verification would require plugs cut in several directions as mentioned earlier, but this would be extremely time consuming, expensive and requires that the rock be homogeneously anisotropic in the interval where all the plugs are cut.

The next stage in our research will be to compare digital rock physics anisotropy predictions with the experimental techniques on some sedimentary rock samples, particularly since the digital rock physics permeability anisotropy module methodology, assumptions and predictions are likely to be more realistic for sedimentary rocks. However, the same verification issues will persist, due to currently not be able to measure the full 3D permeability anisotropy on a single cylindrical plug.

Note that for cubic samples anisotropic measurements of certain parameters (such as permeability or acoustic properties using parallel planar transducers) can only potentially be made in 3 orthogonal directions (e.g., in the X, Y and Z axes). Those directions will not necessarily correspond to the 3 principal anisotropy axes, and thus such measurements will not yield the true principal anisotropy axes unless the 3 orthogonal measurements happen to be exactly co-incident with the 3 principal anisotropy axes.

6 Conclusions

1. Full 3D anisotropy comparisons between μCT image derived rock physics predictions and experimental measurements are reported on exactly the same single core plug sample for the first time (as far as we are aware). Full 3D anisotropy comparisons were made between μCT predicted permeability and measured AIRM and AMS. For μCT predicted s-wave velocity and electrical conductivity anisotropies the determinations were possible along the 3 orthogonal X, Y and Z sample axes, rather than the full 3D anisotropy (i.e., they didn't include off-diagonal components), but nonetheless were consistent with the permeability anisotropy, AIRM and AMS results. The AGRM also gave consistent orientations, as well as the same order of the principal anisotropy axes (max., int. and min) for the SSD ferrimagnetic particles, but this method does not give the absolute magnitudes of those axes. The results from each method were consistent by giving generally closely related orientations for the 3 principal anisotropy axes, and every method indicated that with respect to the sample reference axes Z>X>Y. The results were consistent with the observable petrofabric seen in the core plug images and the μCT images.

2. The 3D principal anisotropy axis orientations of the bulk rock components (via the digital rock predicted anisotropies of permeability and electrical conductivity, as well as both the predicted and measured s-wave velocity anisotropy) were similar to those of the fine-grained ferrimagnetic components (via AIRM, AGRM and AMS).

3. In terms of direct comparisons in the XY plane, the orientations of the maximum (close to the X axis) and minimum (close to the Y axis) anisotropy axes were similar for the measured s-wave velocities, AGRM, AIRM, AMS and predicted permeability. The µCT predicted s-wave velocities and electrical conductivities also gave X>Y, even though the module for these two determinations only considered the X and Y orientations.

4. The results from our sample suggested the potential for estimating the full 3D anisotropy of any one of the parameters from measurements or predictions from any one of the other parameters on single core plugs (e.g., estimating anisotropies of permeability, acoustic velocities or electrical conductivity via rapid, non-destructive magnetic anisotropy measurements).

5. The links between µCT derived anisotropy predictions, experimental anisotropy measurements, and observable petrofabric help to provide validation and confidence in the digital rock physics predictions and the experimental measurement techniques.

6. The different methods used in this study allow the anisotropy of different components (e.g., minerals, pore network via permeability anisotropy, and ferrimagnetic grain size fractions via AIRM) and petrophysical properties to be quantified.

7. Differences in the normalized magnitudes of the principal axes from each method may ultimately be related to specific mineral components or properties, which in turn may relate to particular rock types. This study represents a first step towards elucidating such relationships. Moreover, differences in the magnitudes and orientations of the anisotropies of the various mineral components and/or properties will likely be linked to natural processes, such as flow directions (such as the recent work by [15] estimating paleo-wind directions by combining µCT imaging and AMS), deformation etc.

D. K. P. thanks the Natural Sciences and Engineering Research Council of Canada (NSERC) for a Discovery Grant. Matthias Halisch and Mohammed Ameen are thanked for their constructive review comments, which helped improve the manuscript.

7 List of abbreviations

AF	Alternating Field
AGRM	Anisotropy of GRM
AIRM	Anisotropy of IRM
AMS	Anisotropy of Magnetic Susceptibility
AMR	Anisotropy of Magnetic Remanence
ASWV	Anisotropy of Shear Wave Velocity
CT	Computer Tomography
Dec.	Declination angle
DF	Direct Field
GRM	Gyroremanent Magnetization
Inc.	Inclination angle
IRM	Isothermal Remanent Magnetization
MD	Multidomain
SSD	Stable Single Domain
X, Y, Z	X, Y and Z reference axes of the sample
XY etc	XY plane of the sample
x, y, z	x, y and z components of remanence

8 References

1. S. Zhang, R. E. Klimentidis and P. Barthelemy. Micron to millimetre upscaling of shale rock properties based on 3D imaging and modelling. *Proceedings of the Society of Core Analysts*, 27-30 August, Aberdeen, UK. Paper SCA2012-20 (2012).
2. S. Zhang, A. Byrnes and J. Howard. Property upscaling in porosity systems with under-resolved features using image-based rock physics. *SPE/AAPG/SEG Unconventional Resources Technology (URTEC) Conference*, 22-24 July, Denver, Colorado, USA. DOI: https://doi.org/10.15530/urtec-2019-416 (2019).
3. D. K. Potter. Novel techniques to rapidly determine the magnetic anisotropy of reservoir rocks and shales, and comparisons with permeability and acoustic anisotropies. *Proceedings of the 2011 International Symposium of the Society of Core Analysts, 18-21 September 2011*, Austin, Texas, USA. Paper SCA2011-031 (2011).
4. P. Y. Cholach, J. B. Molyneux and D. R. Schmitt. Flin Flon belt seismic anisotropy: elastic symmetry, heterogeneity, and shear-wave splitting. Canadian Journal of Earth Sciences, **42**, 533-554 (2005).
5. S. Zhang, A. P. Byrnes, J. Jankovic and J. Neilly. Management, analysis, and simulation of micrographs with cloud computing. Microscopy Today, **27** (2), 26-33 (2019).
6. W. M. Telford, L. P. Geldart, R. E. Sheriff and D. A. Keys. *Applied Geophysics (2nd Edition)*. New York, NY : Cambridge University Press, pp. 770 (1990).
7. O. L. Anderson and R. C. Liebermann. Sound velocities in rocks and minerals. *VESIAC State-of-the-Art Report (Accession Number : AD0804865)*, pp.182 (1966).
8. A. Ali, S. Abdalah and D. K. Potter. Quantifying the role of grain lining hematite cement in controlling permeability in a relatively tight gas sandstone reservoir from the North Sea. SPE Reservoir Evaluation and Engineering, **15**, Issue 6, 618-623 (2012).
9. A. Stephenson, S. Sadikun and D. K. Potter. A theoretical and experimental comparison of the anisotropies of magnetic susceptibility and remanence in rocks and minerals. Geophysical Journal of the Royal Astronomical Society, **84**, 185-200 (1986).
10. D. K. Potter. A comparison of anisotropy of magnetic remanence methods – a user's guide for application to paleomagnetism and magnetic fabric studies. In *"Magnetic Fabric: Methods and*

Applications." Martin-Hernandez, F., Luneburg, C. M., Aubourg, C. and Jackson, M. (eds.), Geological Society, London, Special Publications, **238**, 21-35 (2004).

11. A. Stephenson. Gyroremanent magnetization in anisotropic magnetic material. Nature, **284**, 49-51 (1980).
12. A. Stephenson and D. K. Potter. Gyroremanent magnetizations in dilute anisotropic dispersions of gamma ferric oxide particles from magnetic recording tape. IEEE Transactions on Magnetics, MAG-**23**, 3820-3830 (1987).
13. D. K. Potter and A. Stephenson. Single-domain particles in rocks and magnetic fabric analysis. Geophysical Research Letters, **15**, 1097-1100 (1988).
14. B. C. Snow. Nanoparticle magnetic characterization and comparison of rock anisotropy methods. MSc thesis, University of Alberta, pp. 95 (2018).
15. M. Halisch, C. Zeeden and C. Rolf. Towards image based assessment and characterization of cyclic paleo-wind and flow fields. *European Geoscience Union Assembly*, 4-8 May, 2020, Vienna, Austria (2020).